SPECTROSCOPY OF A TRAPPED ION IN A STANDING WAVE

A Thesis
Presented to
The Academic Faculty

by

Karl A. Burkhardt

In Partial Fulfillment
of the Requirements for the Degree
Bachelor of Science in the
School of Chemistry and Biochemistry

Georgia Institute of Technology
May 2014

SPECTROSCOPY OF A TRAPPED ION IN A STANDING WAVE

Approved by:

Kenneth R. Brown, Advisor
Schools of Chemistry and Biochemistry,
Computational Science and Engineering,
and Physics
Georgia Institute of Technology

Lawrence A. Bottomley
School of Chemistry and Biochemistry
Georgia Institute of Technology

Date Approved: 3 May 2013

To my loving family and my lovely fianceé

"Theory guides, experiment decides."

- Izaak Kolthoff

"The theory of quantum mechanics ... explained all kinds of details, such as why an oxygen atom combines with two hydrogen atoms to form water, and so on. Quantum mechanics thus supplied the theory behind chemistry. So, fundamental theoretical chemistry is really physics."

- Richard Feynman, "QED: The Strange Theory of Light and Matter"

ACKNOWLEDGEMENTS

First and foremost, I must express my gratitude to Ken Brown for taking a chance on me and allowing me to perform research in his lab. The first semester I was in the Brown Lab Ken was on his "tenure tour," and was rarely in Atlanta. Even with his busy schedule, he still made time to meet with the lowly first-semester undergrad in his lab in order to teach me quantum mechanics. From that semester on he has always made himself available for consultation and our conversations are never limited to research. Ken taught me to pursue the areas of science I find interesting, regardless of their labeled classification or how they are popularly received.

Alexa Harter and Curtis Volin were the motivation that I needed during my time at GTRI. They were always excited about new results and ever optimistic, even when it felt like the experiment was falling apart.

James Goeders and Grahame Vittorini were the two graduate students I had the pleasure of working with the most. When I started in the Brown Lab, I worked on the cold molecular ions project with James. My fondest Brown Lab memory will always be staying up until 2 a.m. staring at a pressure gauge while James leaked oxygen into the chamber through the broken leak valve. When I switched to the cryogenic ion trap project that Grahame was in charge of I never thought I would be able learn so much in such a short period of time, but Grahame was a great teacher and remained a great resource even after his graduation.

Jason Amini helped me way more than he ever needed to or ever should have. He took me to the white board to blow my mind many different times and I would not have been able to get the results I did if it was not for his help.

In addition to Ken, James, and Grahame, every Brown Lab member has been helpful and supportive in some way, shape, or form; even the theorists feigned interest when I

talked about experimental difficulties. Specifically, I would like to thank Ncamiso (JB) Khanyile, Gang (Rick) Shu, John Gray, Brian McMahon, René Rugango, Chien-Yuan (Ted) Chang and Rob Clark for sharing their experimental knowledge with me.

In addition to Curtis, Alexa, and Jason, I am grateful to many other QIS members for their time and patience. Kenton Brown has taught me about electronics, True Merill has explained the theory of trapped ions to me, and Spencer Fallek, Nicholas Guise, and Tom Delaubenfels have all taught me about lasers and other trapped ion experiments.

Many different teachers have molded my scientific interests over the years. These include: Randi Collier, Mark Stevens, Gary Schuster, Carrie Shepler, Christine Payne, Larry Bottomley, David Sherill, and Turgay Uzer.

My parents and sister have been so supportive of me and my education, regardless of the field; they started my interest in science and how the world works and provided me all the tools necessary for success. My grandparents have also been a huge part of my life and always encouraged my questions when I was younger, even when I was inevitably being an annoying kid.

Finally, my fianceé Jennifer Curington has been there with me through every step of college. She encouraged me when I needed encouragement and was always willing to listen when I just needed to vent about misbehaving lasers.

TABLE OF CONTENTS

LIST OF TABLES

LIST OF FIGURES

SUMMARY

With the recent surge for an experimentally viable quantum computer, trapped ions have come to the forefront as one of the most practical systems from which to construct a quantum computing architecture. This work has continued to explore the feasibility of using trapped ions as quantum bits, addressing the issue of quantum decoherence due to non-resonant excitation by studying the spectroscopy of a trapped ion through a standing wave.

The standing wave studied in this thesis was formed on the face of a surface-electrode ion trap held at cryogenic temperatures. Although the trap was not built with a reflective surface in mind, a lower bound on the fringe visibility was measured to be 0.717. By moving the ion through the nodes and anti-nodes of the wave, the carrier and sidebands of the $S_{1/2} \rightarrow D_{5/2}$ transition, commonly used for information storage, were selectively stimulated and suppressed.

CHAPTER I

INTRODUCTION

Through use of frequency stabilized lasers the energy levels of a trapped ion can become hydrogen-like in that they have a simple structure. By using these lasers to cool an ion to its Doppler limit, a near perfect two level approximation can be made. It is the formation of this two level system, and the ability to reliably detect the state of the ion, that gives trapped ions the ability to act as quantum bits (qubits).

1.1 Motivation for Quantum Computation

In 1982, Richard Feynman proposed the idea that a quantum mechanical system would be best modeled with a quantum computer rather than a classical computer [1]. It was not until 1994 however, when Peter Shor proposed his prime factorization algorithm, that much attention was given to the idea of quantum computation [2]. Since then, other quantum algorithms have been formulated that are capable of searching through databases more efficiently than classical computers [3] and performing quantum chemical calculations [4]. Enough interest in quantum computation was generated from Shor's algorithm that the next year Ignacio Cirac and Peter Zoller proposed a way in which to implement a two qubit gate on a linear chain of trapped ions in a paper that started the field of trapped ion quantum computation [5].

1.2 Trapped Ion Quantum Information

Prior to the proposal made by Cirac and Zoller, trapped ions had been used for a variety of applications, including precise spectroscopic measurements [6], frequency standards and clocks [7, 8], tests of fundamental quantum mechanics [9, 10], and tools with which to search for spin dependent forces [11]. However, after their proposal, many ion trapping

groups changed their focus toward the implementation of quantum gates for quantum computation.

Although the Cirac-Zoller gate has been performed on linear chains of trapped ions [12, 13], the ability to perform quantum gates alone is not enough to build a quantum computer. In addition to having a universal set of quantum gates, a complete quantum computer architecture constructed from trapped ion qubits must also possess well-characterized qubits with long coherence times, qubit specific measurements, and the ability to transport qubits between pre-determined locations [14]. To go about building this trapped ion system, the distance between the trap electrodes and the ions will need to be on the order of 10 μm [15] and the trap must be able to transport the ions in a fast (relative to gate operation times) manner [16, 17].

While progress has been made toward these landmarks, a fully functional quantum computer based on trapped ion qubits has yet to be experimentally realized. To provide a two dimensional landscape around which the ions can be transported, researchers from the National Institute of Standards and Technology proposed a new alternative to the traditional linear Paul trap: A surface-electrode ion trap [18]. This type of trap not only allows for ions to be transported in two dimensions, but also has the potential to decrease the distance between the ion and the electrodes. Unfortunately, this decrease in distance increases the heating of the ions [19] resulting in shorter coherence times. To overcome this increase in heating, new experimental techniques must be realized.

1.3 Reduction of Ion Heating

To address the higher heating rates and shorter lifetimes observed in surface-electrode ion traps, high speed vacuum pumps such as titanium sublimation pumps or non-evaporable getters can be placed in close proximity to the ion to decrease the local pressure [20]. In addition to reducing elastic collisions between the ion and background gas molecules that cause heating, these pumps also reduce inelastic collisions where charge-exchange or

chemical reactions may occur [21]. To further reduce heating beyond what high speed vacuum pumps alone are able to achieve, the surface of a trap is able to be cleaned using a process known as argon ion milling. By removing surface contaminants such as carbon on the radio frequency (rf) rails used to create the trapping pseudopotential, the heating due to fluctuating patch potentials is reduced. This process has been shown to decrease the heating rate of a trap by two orders of magnitude [22].

It has also been shown that cooling surface-electrode ion traps to cryogenic temperatures decreases ion heating relative to similar ion traps at room temperature [15, 23, 24]. The cryogenic temperatures serve to both suppress anomalous heating due to fluctuating patch potentials and decrease the pressure around the ion [25]. This decrease in pressure due to cryopumping reduces the need for other vacuum systems once the system is at sufficiently cold temperatures. Because of these advantages, a new, modular, cryogenic chamber, shown in Fig. 1, has been constructed through a collaboration between the Brown Lab at the Georgia Institute of Technology and the Quantum Information Systems Group at the Georgia Tech Research Institute [26]. This chamber houses a surface-electrode ion trap and has not only shown an order of magnitude decrease in ion heating in an identical trap held at room temperature, but an order of magnitude increase in the lifetimes of uncooled ions has also been observed. Because of these factors, this cryogenic chamber is an ideal place to perform studies on potential nonlinear heating in ion traps, implement two qubit gates, and perform heating sensitive measurements.

1.4 Applications of a Trapped Ion in a Standing Wave

The work contained in this thesis has attempted to advance the field of trapped ion quantum computation by studying the motion of a trapped ion through a standing wave formed on the surface of a GTRI Gen. II surface-electrode trap [27]. This trap is operated in the cryogenic chamber described in Ref. [26] and shown in Fig. 1.

Having trapped a $^{40}Ca^{+}$ ion in the Gen. II surface-electrode trap shown in Fig. 2, a 729

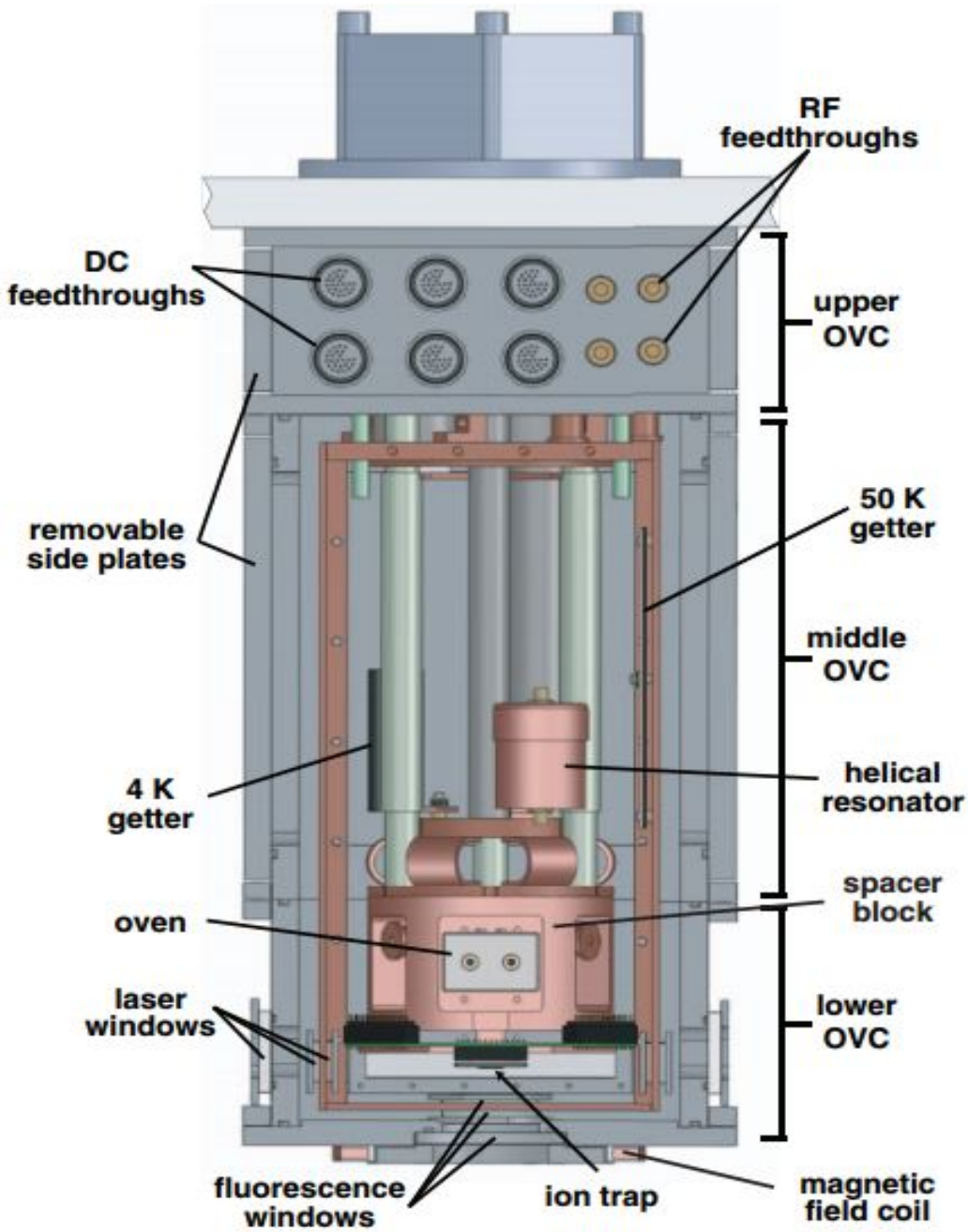

Figure 1: A schematic of the liquid helium cryogenic chamber in which the experiments discussed in this thesis were performed.

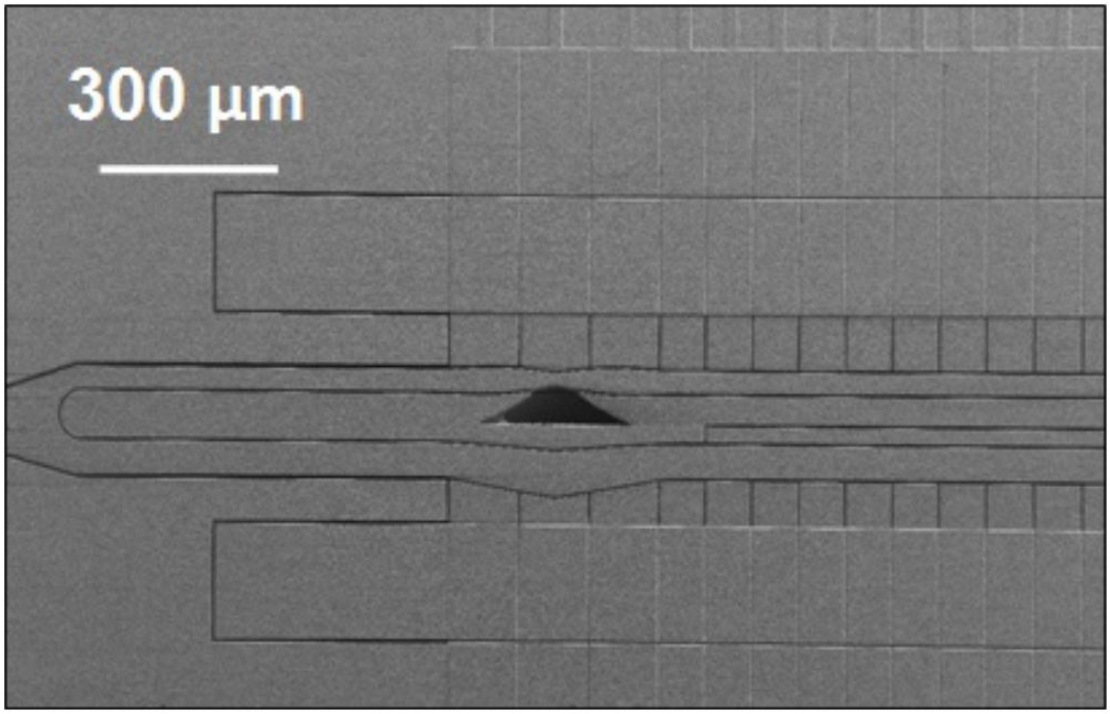

Figure 2: Optical microscope image of a GTRI Gen. II surface-electrode ion trap. The experiments discussed in this thesis were performed in a Gen. II trap identical to the one shown here.

nm laser used to address the $S_{1/2} \rightarrow D_{5/2}$ transition can be oriented perpendicular to the plane of the trap as shown schematically in Fig. 9. By applying compensation voltages to the center trap electrode, the ion is pushed through the nodes and anti-nodes of the standing wave. In moving the ion through the nodes and anti-nodes, the carrier and sidebands of the $S_{1/2} \rightarrow D_{5/2}$ transition are able to be selectively stimulated or suppressed.

This selective stimulation and suppression will help to perform fast two qubit gates with specific application to the Cirac-Zoller gate. Traditionally, two problems have arose while trying to implement the Cirac-Zoller two qubit gate. The first is that the chain of ions acting as qubits is very sensitive to heating and must be in the motional ground state before the Cirac-Zoller gate can be performed [5]. The second is that the Rabi rate of the first order blue sideband is slow relative to the decoherence times of the two qubits. By performing a Cirac-Zoller gate in a cryogenic chamber, much of the noise that gives rise to heating would be frozen, helping to solve the first problem [15, 23, 26]. The second problem could

be solved by placing the ions in a standing wave and changing the position of the ions to suppress the carrier and even order sidebands while the first order blue radial sideband is addressed. This would allow more power with which to excite the first order blue radial sideband without non-resonantly exciting the carrier or second order blue sideband. Since the Rabi frequency scales with $\sqrt{I}$ [28], where I is the intensity of the seeding radiation, this would allow for faster first order blue radial sideband Rabi oscillations, helping to decrease the Rabi rate and thus decrease the likelihood of the state of the qubit to decohere due to both trap heating and off-resonant excitation.

Potentially even more exciting than the possibility of faster two-qubit gates is the physical interpretation of the selective suppression of carrier or sideband transitions. What this means is that the Hamiltonian of the system is able to be changed in a selective manner. Using this modified Hamiltonian, certain quantum simulation proposals, most notably Ref. [29], should be able to be performed.

In Ref. [29] it is asserted that a frequency scan of the 729 nm laser over the $S_{1/2} \rightarrow D_{5/2}$ transition of a trapped Ca^+ ion with a suppressed carrier would act as an analogue test of quantum field theory effects in an expanding universe. Were this scan to be produced, and it should be possible with the standing wave described in Section 2.4, the quantum effects of cosmological expansion will be able to be modeled and cosmologists will be able to better understand curved-spacetime quantum field theory effects such as the Gibbons-Hawking effect in de Sitter spacetime [30] and the entanglement signature of de Sitter spacetime [31].

CHAPTER II

METHODS AND MATERIALS

This section focuses on the spectroscopy of trapped ions and their uses as qubits rather than the details and mechanics of ion trapping. For an in depth analysis of ion traps the reader is encouraged to examine outside sources such as Ref. [32, 33, 34, 35]. Specifically, Ch. 2 of Ref. [34] and Ch. 11 of [35] have been of great use to the author.

2.1 Trapping Methods

The experiments outlined in this thesis were performed in a custom built cryogenic chamber [26] under ultra-high vacuum. To load the ions into the trap, a calcium containing oven inside the cryogenic chamber is resistively heated such that a thermal flux of calcium atoms pass through the loading zone of the GTRI Gen. II surface-electrode ion trap [27]. Focused above the loading zone are two photoionization lasers, a 423 nm laser resonant with the $4s^2\ {}^1S_0 \rightarrow 4s4p\ {}^1P_1$ transition of ^{40}Ca and a non-resonant 377 nm laser used to promote the electron to the continuum after excitation [36]. Upon photoionization, the $^{40}\mathrm{Ca}^+$ ion is confined by the quadrupole pseudopotential created by the oscillating rf field applied to the trap. Upon trapping the photoionized calcium atom, the $S_{1/2} \rightarrow P_{1/2}$ transition is addressed and the ion is cooled to its Doppler limit. Once at the Doppler limit, the trap is compensated so that the ion sits at the pseudopotential null and experiments are able to be performed [37].

2.1.1 Calcium Isotopes and their Energy Level Structure

Although the work contained in this thesis is primarily concerned with $^{40}\mathrm{Ca}^+$, future applications and experiments hope to involve other isotopes of calcium. For this reason, Appendix A is included.

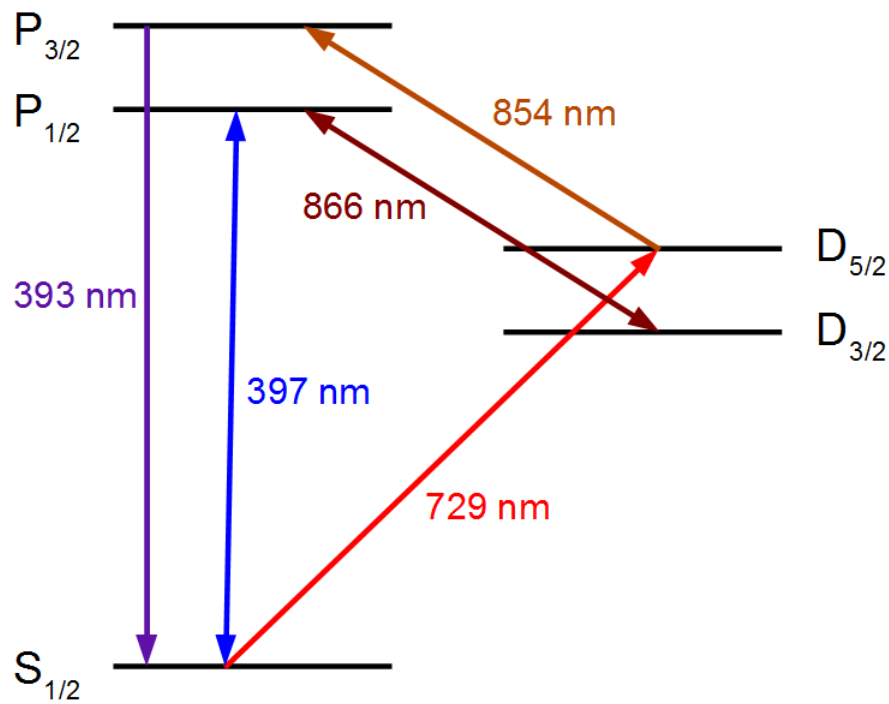

Figure 3: Partial Jablonski diagram showing all of the relevant energy levels for laser cooling Ca^+.

A partial Jabolnski diagram showing the relevant energy levels for Doppler and sideband cooling are shown in Fig. 3. The 729 nm transition detuning included in Table 1 was calculated by closing the energy loop shown in Fig. 3 for each isotope and solving for the frequency of the $S_{1/2} \rightarrow D_{5/2}$ transition. The calculation of the $S_{1/2} \rightarrow D_{5/2}$ shift for the $^{44}Ca^+$ isotope is shown in Appendix A. All other isotopes were calculated in a similar manner, substituting their own respective shifts from the data provided in Ref. [36].

The only experimental value of the 729 nm $S_{1/2} \rightarrow D_{5/2}$ transition for an isotope other than $^{40}Ca^+$ currently available in the literature is for $^{43}Ca^+$ and is found in Ref. [38]. According to this reference, the value of the calculated $S_{1/2} \rightarrow D_{5/2}$ shift for $^{43}Ca^+$ is off by only 19 MHz, or an error of 0.46%.

2.2 *Laser Cooling*

By stimulating electronic transitions with a laser, a trapped ion can be cooled first to its Doppler limit, and then to its motional ground state within the trap. The first process is known as Doppler cooling while the latter is known as sideband cooling.

2.2.1 Doppler Cooling

Doppler cooling is only possible if the electronic states of the probed species, in this case the trapped ion, form a closed cycling transition. A dipole allowed transition ($\Delta L = \pm 1$) is most commonly used to reach the Doppler limit, although a dipole forbidden transition ($\Delta L \neq \pm 1$) lowers the temperature of the particles at their Doppler limit [39]. Doppler cooling on a power broadened quadrupole transition ($\Delta L = \pm 2$) such as the $S_{1/2} \rightarrow D_{5/2}$ transition for a trapped Ca^+ ion has potential applications in low noise state detection, but the cooling rate is too slow to keep the ions trapped for extended periods of time [40]. Since the experiments described in this thesis used Doppler cooling to cool a thermal $^{40}Ca^+$ ion, a dipole allowed transition was addressed. For trapped Ca^+ ions, both a tunable 397 nm laser to couple the $S_{1/2}$ and $P_{1/2}$ states and a 866 nm laser to repump from the metastable $D_{3/2}$ state are required in order to reach the Doppler limit. An illustration showing the detuning of the 397 nm laser and the coupling of the $P_{1/2}$ and $D_{3/2}$ states is shown in Fig. 4.

After the ion has been cooled to its Doppler limit, it is in the Lambe-Dicke regime and its temperature is only a few millikelvin [41]. Once the ion is in the Lambe-Dicke regime, it is able to be sideband cooled to its motional ground state [42].

2.2.2 Sideband Cooling

In the case of a trapped Ca^+ ion, the motional ground state is reached by probing the quadrupole $S_{1/2} \rightarrow D_{5/2}$ transition. A dipole forbidden transition is required because the linewidth of the transition must be much less than the rf drive frequency of the trap. For the trap used in these experiments, the rf drive frequency is 47.846 MHz. By detuning the

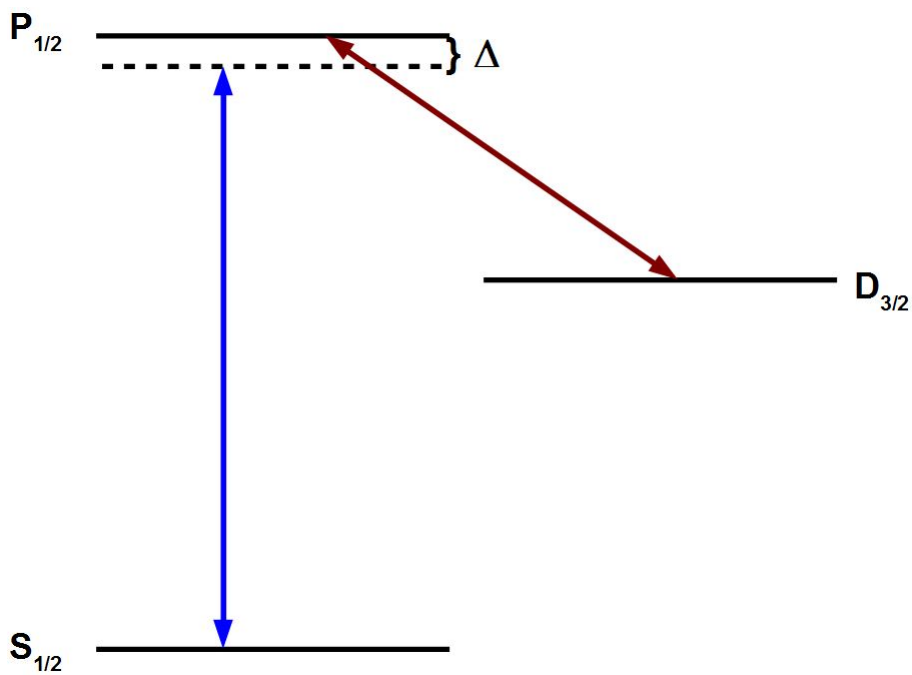

Figure 4: Doppler cooling illustration. The $S_{1/2}$ and $P_{1/2}$ states are coupled with a laser red detuned by Δ such that the emitted photons are higher in energy than the absorbed photons.

frequency of the 729 nm laser that couples the $S_{1/2}$ and $D_{5/2}$ states by the trap frequency ω, on average, one motional quanta is removed from the ion with each cycle [43]. For the trap used in these experiments, the trap frequency is on the order of 1 MHz [44, 20]. This cooling cycle is shown schematically in Fig. 5.

By addressing the $S_{1/2} \rightarrow D_{5/2}$ transition with the 729 nm laser detuned by the trap frequency ω, one motional quanta is removed when the electron is promoted to the $D_{5/2}$ state. To pump the electron back to the $S_{1/2}$ state, the ion is addressed with a 854 nm laser to drive the $D_{5/2} \rightarrow P_{3/2}$ transition where the motional quantum number n remains the same as it was in the $D_{5/2}$ state. Upon spontaneous emission to the $S_{1/2}$ state the motional quantum number is able to change by +1, 0, or -1, all with equal probability. On average, the ion will lose one motional quanta per cycle. By cycling many times, the ion is able to be cooled to its motional ground state where $n = 0$ [43].

Through the process of sideband cooling the motional ground state is able to be achieved.

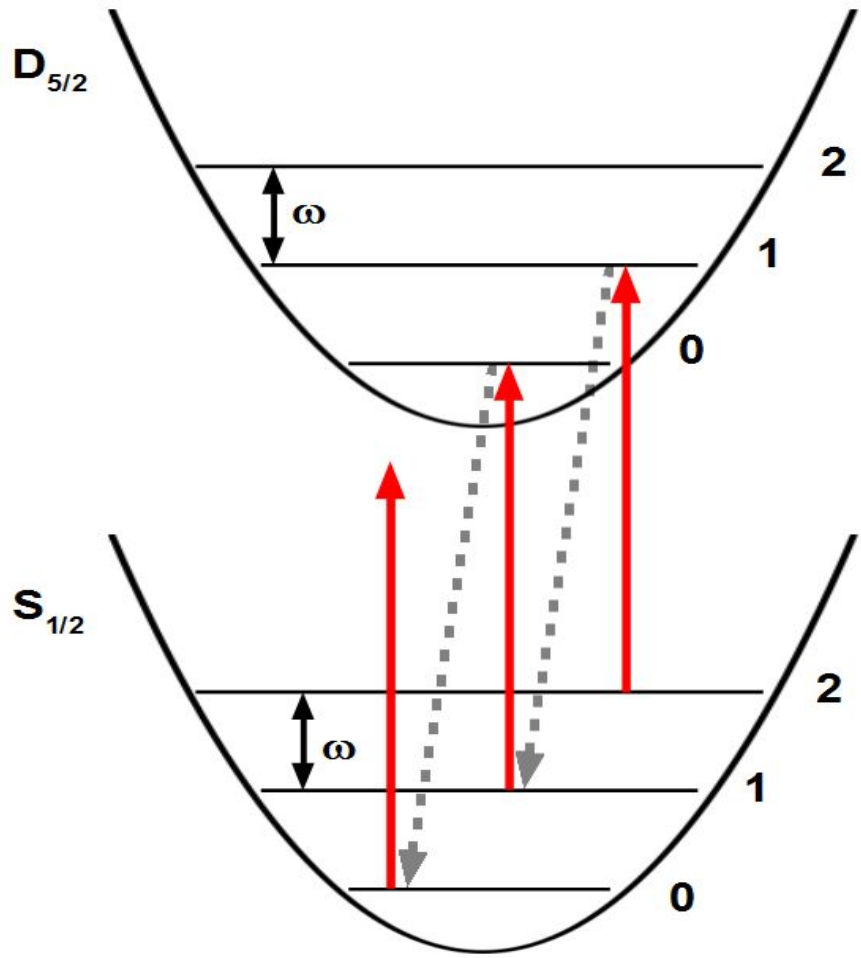

Figure 5: Schematic demonstration of sideband cooling. The red arrows represent the 729 nm laser which is detuned from resonance by the trap frequency ω. The dashed gray arrows represent the stimulated $D_{5/2} \rightarrow P_{3/2}$ absorption and the spontaneous decay back into the $S_{1/2}$ state where, on average, the motional quantum number will remain the same as in the $D_{5/2}$ state. Once the ion is in the motional ground state, the energy of the laser will no longer be enough to couple the $S_{1/2}$ and $D_{5/2}$ levels so the electron will be stuck in the $S_{1/2}$ state with a motional quantum number of $n = 0$.

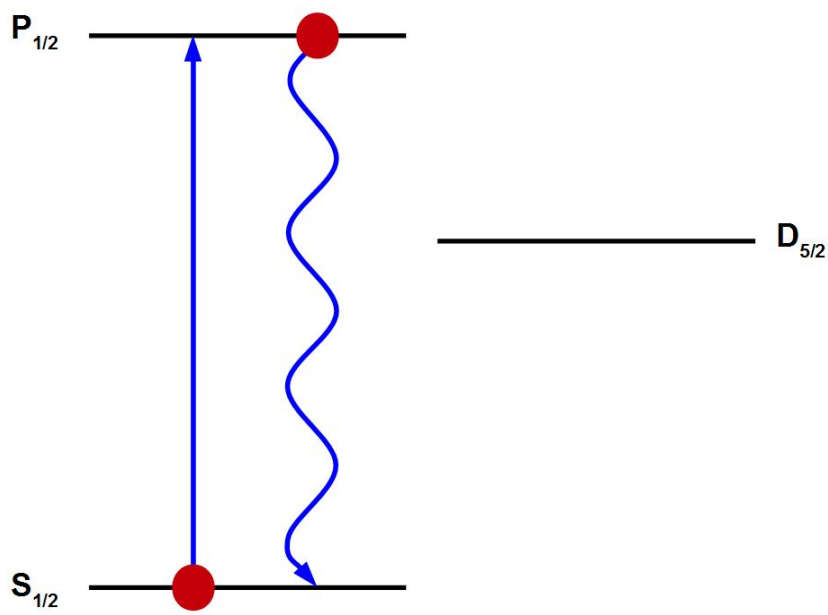

Figure 6: If the electron is collapsed into the $S_{1/2}$ state, fluorescence will be observed by driving the $S_{1/2} \rightarrow P_{1/2}$ transition.

In this state, quantum computation operations are able to be performed with better coherence compared to operations performed on ions that have only been cooled to their Doppler limit [16].

2.3 State Detection

Having cooled the ion, it is important to be able to determine the state of the qubit for quantum computation applications. Because of the limited number of energy levels accessible to the ion, the state can always be detected using laser induced fluorescence (LIF). By leaving the 866 nm laser turned on at all times during experiments, it is guaranteed that the electron will never be in the $D_{3/2}$ state for more than a few nanoseconds. This, coupled with the nanosecond lifetimes of the $P_{1/2}$ and $P_{3/2}$ states [45], means that the electron can only be in the $S_{1/2}$ or $D_{5/2}$ states for extended periods of time. It is for this reason that a two-level approximation can be made and the ion can be treated as a qubit.

Since the electron can always be collapsed into either the $S_{1/2}$ or $D_{5/2}$ state, the state of the ion can be determined with near 100% efficiency using LIF on the $S_{1/2} \rightarrow P_{1/2}$ transition

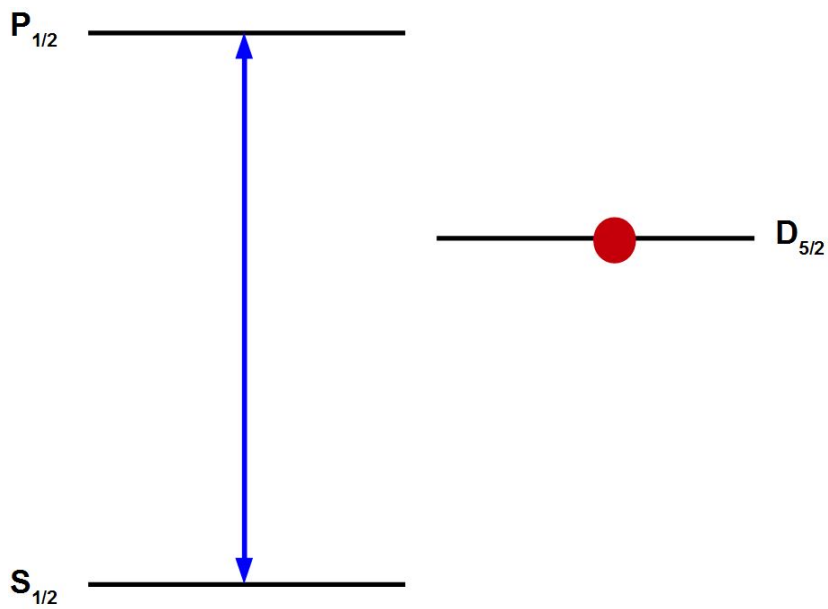

Figure 7: If the electron is collapsed into the $D_{5/2}$ state, fluorescence will not be observed when the $S_{1/2} \rightarrow P_{1/2}$ transition is driven.

[21]. If the wavefunction is made to collapse into the $S_{1/2}$ state while the 397 nm laser is pulsed then fluorescence will be observed. However, if the wavefunction is made to collapse into the $D_{5/2}$ state while the 397 nm laser is pulsed, then no fluorescence will be observed. Cartoon demonstrations of these two respective processes are shown in Fig. 6 and 7.

The light scattered from the ion during LIF is spread over a full 4π solid angle, of which only about 4% is caught using the home-built NA 0.4 lens stack [20]. The lens stack feeds into a 50/50 beamsplitter which then feeds into both a CCD camera (Princeton Instruments Cascade 1K) and a photomultiplier tube (PMT; Hamamatsu H10682-210). The camera is used for laser alignment and visual feedback while the PMT is used for state detection. The fluorescence collection optics along with the y-axis 729 nm laser used to form the standing wave described in Section 2.4 are shown in Fig. 8.

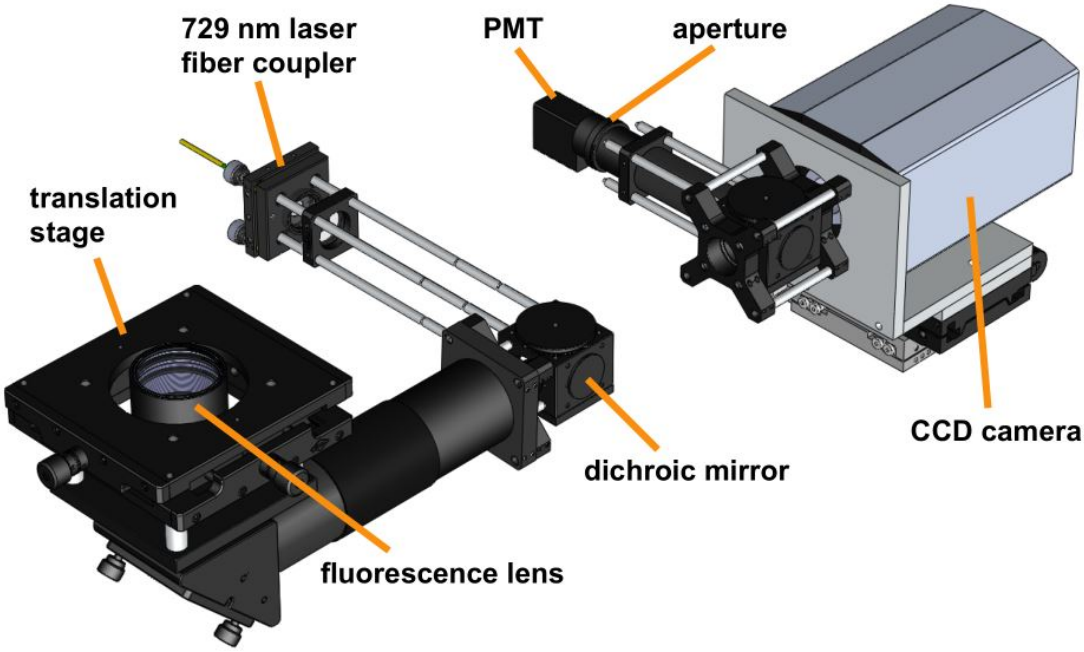

Figure 8: Light collection optics used for state detection and ion positioning as well as the 729 nm laser used to form the standing wave described in Section 2.4. Reproduced from Ref. [20].

2.4 729 nm Standing Wave

After the ion has been trapped and transported to the center of the trap as described in Ref. [27], a standing wave is able to be formed on the surface of the trap with the 729 nm laser. Using the y-axis 729 nm laser shown in Fig. 8, the radiation reflected off the aluminum surface of the trap creates evenly spaced points every 365 nm (729/2 nm) where the electric field is greatly decreased [46]. Under ideal circumstances the electric field would drop to 0 at these nodes and the interferometric visibility of the wave would be 1, but the surface of the ion trap used in these experiments is not a perfect mirror and so the interferometric visibility is less than 1. A cartoon showing the idealized electric field at the ion is shown in Fig. 9.

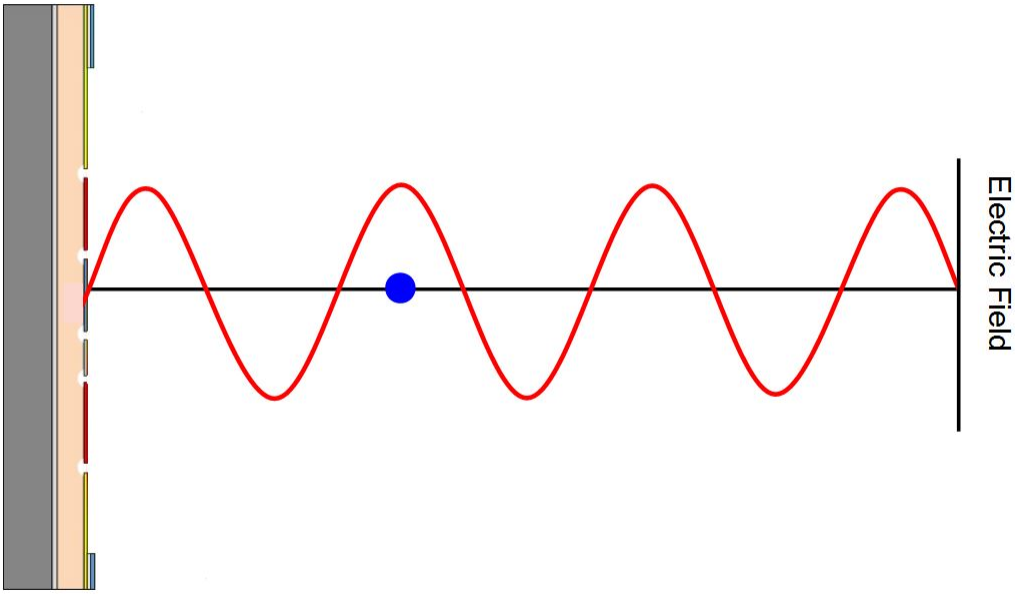

Figure 9: An idealized standing wave formed on the surface of the GTRI Gen. II surface-electrode ion trap used in this experiment.

CHAPTER III

SPECTROSCOPIC RESULTS

Having cooled the ion to its Doppler limit, the transition resonance peaks are sharp relative to the Doppler broadened peaks observed in room temperature spectroscopy experiments. For this reason, ion traps with laser cooled ions make excellent precision spectroscopy tools for use in the fields of physics and chemistry alike.

3.1 $^{40}Ca^{+}$ transitions and light collection

In its ground electronic state, a trapped $^{40}Ca^{+}$ ion with $+1/2$ spin exists in the $S_{1/2}$ state. This can be seen through examination of Fig. 3 where the $S_{1/2}$ state is the lowest lying electronic state. From the $S_{1/2}$ state, only two dipole allowed transitions can occur, the $S_{1/2} \rightarrow P_{1/2}$ and $S_{1/2} \rightarrow P_{3/2}$ transitions, and only two quadrupole transitions can occur, the $S_{1/2} \rightarrow D_{3/2}$ and $S_{1/2} \rightarrow D_{5/2}$ transitions.

In the interest of reducing the number of lasers required to close the energy loop in order to achieve a two level system, the $S_{1/2} \rightarrow P_{3/2}$ transition is not addressed. This leaves the dipole allowed $S_{1/2} \rightarrow P_{1/2}$ transition which is addressed through use of a 397 nm diode laser. To ensure no coupling of the $D_{3/2}$ and $P_{1/2}$ states with the 866 nm laser (which is left on constantly throughout the course of experiments), the $S_{1/2} \rightarrow D_{3/2}$ transition is not addressed. Rather, the quadrupole allowed $S_{1/2} \rightarrow D_{5/2}$ transition is addressed with a 729 nm diode laser.

Using the collection optics shown in Fig. 8, approximately 2% of the photons scattered from the ion are collected and funnelled into the PMT [20]. By monitoring the current of the PMT and knowing the current-to-photon conversion, the number of photons striking the PMT at any point in time can be calculated.

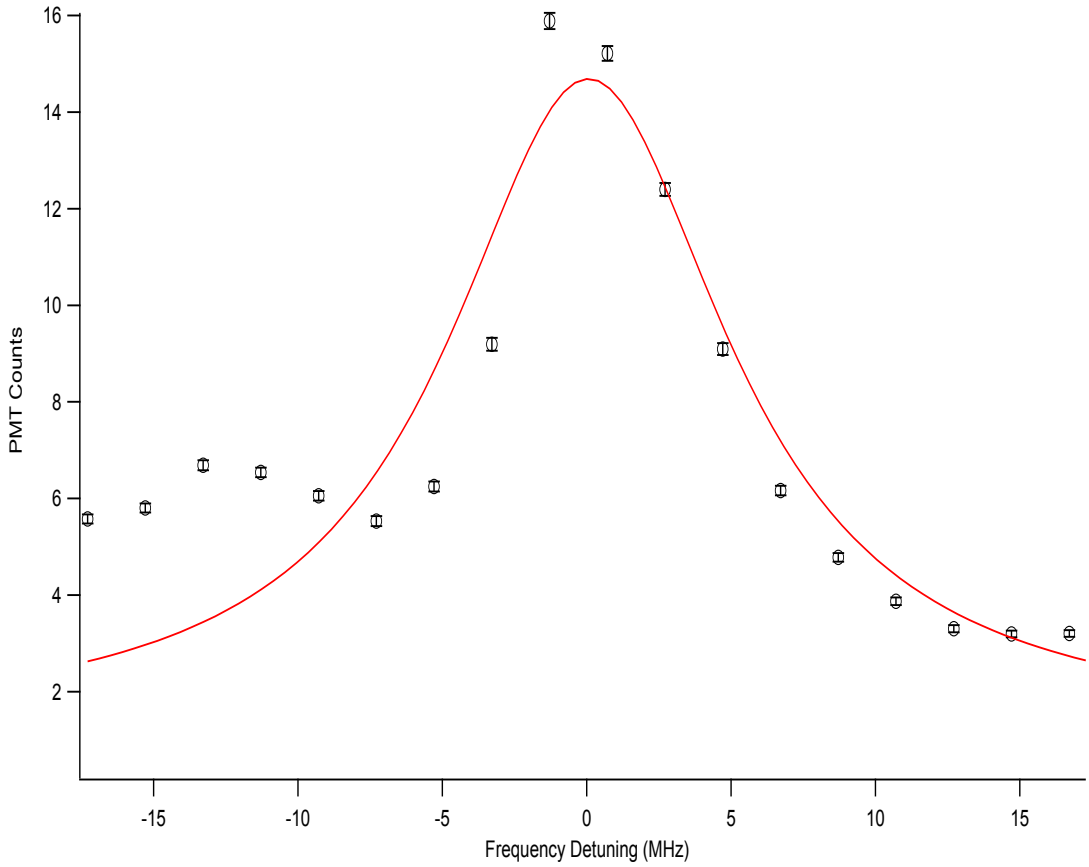

Figure 10: Fluorescence vs. 397 nm laser detuning for the $S_{1/2} \rightarrow P_{1/2}$ transition of $^{40}Ca^{+}$ with a Lorentzian fit.

3.2 Spectroscopy of the $S_{1/2} \rightarrow P_{1/2}$ Line of $^{40}Ca^{+}$

To find the resonant frequency of the $S_{1/2} \rightarrow P_{1/2}$ transition, the frequency of the laser is tuned using an acousto-optical modulator (AOM) while the current of the PMT is monitored. By plotting the number of photons striking the detector per unit time vs. the l;aser frequency, the resonant frequency of the transition is found as shown in Fig. 10. To reduce the linewidth of the transition, the ion was cooled to the Doppler limit before the laser was tuned to the frequency of interest and the fluorescence was observed.

Because the Brimrose AOMs used in these experiments have different power transmittance values over the range of frequencies probed in the $S_{1/2} \rightarrow P_{1/2}$ scans [47], a technique known as power locking is used. At high laser powers and without power locking the LIF laser the PMT response can potentially be a measure of the background laser scatter rather

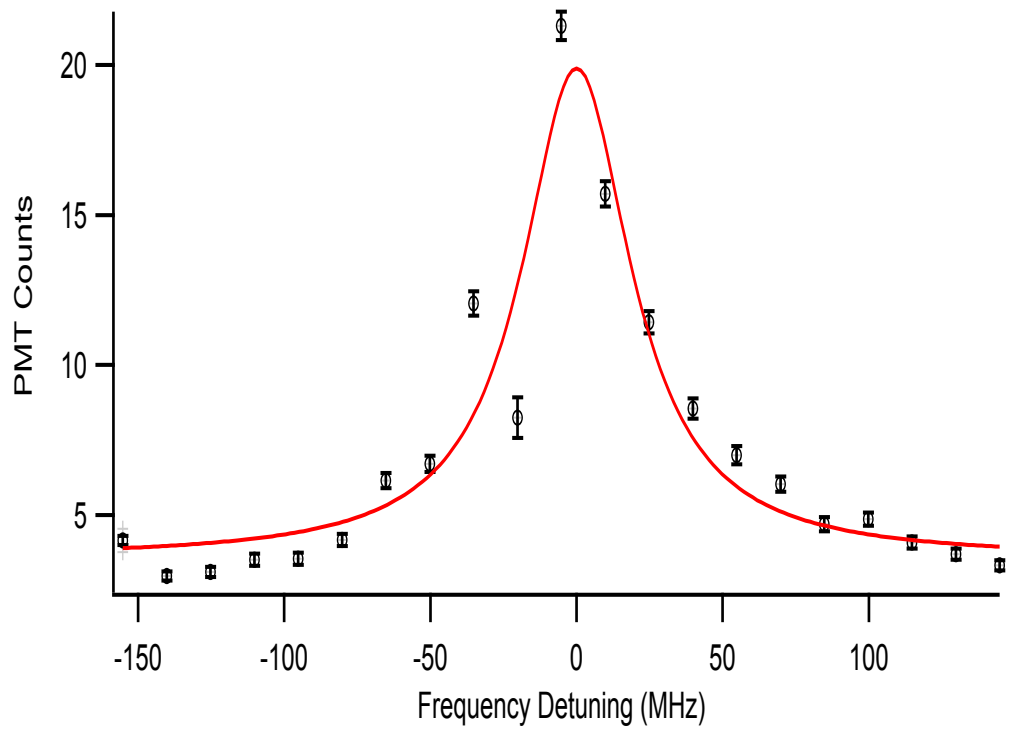

Figure 11: Frequency scan of the $D_{3/2} \rightarrow P_{1/2}$ transition where 397 nm fluorescence is monitored vs. detuning of the 866 nm laser. The data is fit to a Lorentzian.

than a measure of ion fluorescence. To ensure that the PMT response is a function of ion fluorescence rather than background scatter the power of the LIF laser is monitored using a photodiode and locked to a setpoint value. When the power is above or below this setpoint the amplitude of the AOM drive frequency is changed in order to ensure that the power of the LIF laser remains constant over the range of frequencies scanned.

3.3 Spectroscopy of the $D_{3/2} \rightarrow P_{1/2}$ Line of $^{40}Ca^{+}$

In the same manner as the $S_{1/2} \rightarrow P_{1/2}$ transition, the $D_{3/2} \rightarrow P_{1/2}$ transition is measured by scanning the frequency of the 866 nm laser while measuring the 397 nm fluorescence of the ion using the PMT (Fig. 11). In this case however, the 866 nm laser is not what causes the ion to fluoresce at the observed wavelength. Rather, the 866 nm laser pumps the electron out of the $D_{3/2}$ state while the 397 nm laser is tuned to resonance and causes the observed fluorescence.

Given that the 397 nm laser is tuned close to resonance while the 866 nm laser is being modulated, monitoring the 397 nm fluorescence while taking the $D_{3/2} \rightarrow P_{1/2}$ scan still gives a true indication of the resonant peak. As can be seen in Fig. 11, if the 866 nm laser is detuned significantly and the $D_{3/2} \rightarrow P_{1/2}$ transition is not well coupled, less $P_{1/2} \rightarrow S_{1/2}$ fluorescence is detected.

It should be noted that the dip observed in Fig. 11 at approximately −20 MHz is known as the electromagnetically induced transparency (EIT) dip and is due to interference between the dipole moment of the $S_{1/2} \rightarrow P_{1/2}$ and $D_{3/2} \rightarrow P_{1/2}$ transitions [48, 49]. Although the EIT dip increases the difficulty of finding the resonant frequency of the $D_{3/2} \rightarrow P_{1/2}$ transition (an error made in the measurement of the frequency shift of this transition in Ref. [36] could be a possible explanation of the 0.46% error observed in the calculation of the $S_{1/2} \rightarrow D_{5/2}$ shift for $^{43}Ca^{+}$ mentioned in Appendix A), EIT of a trapped ion has the potential to benefit the field of trapped ion quantum computation. Specifically, it has been recognized that EIT has many potential advantages concerning the long-term storage of coherent quantum information [49]. In addition to the storage of information, EIT can be used to cool singly trapped ions [50] as well as trapped ion chains [51, 52] to the motional ground state allowing for better state preparation of chains of ions which is crucial for many two qubit gates [16].

3.4 Spectroscopy of the $S_{1/2} \rightarrow D_{5/2}$ Line of $^{40}Ca^{+}$

For the quadrupole $S_{1/2} \rightarrow D_{5/2}$ transition, also known as the qubit transition for trapped $^{40}Ca^{+}$ ions, sidebands are able to be seen if the scan covers a wide enough frequency range. These sidebands are due to the discrete spacing of the motional modes of the ion within the quantum harmonic oscillator pseudopotential illustrated in Fig. 5. As can be seen in Fig. 12, the spacing of the axial sidebands is on the order of 1 MHz, which is in good agreement with the calculated values provided for the trap given in Ref. [44].

If only a small frequency range is scanned, then only the carrier transition is shown,

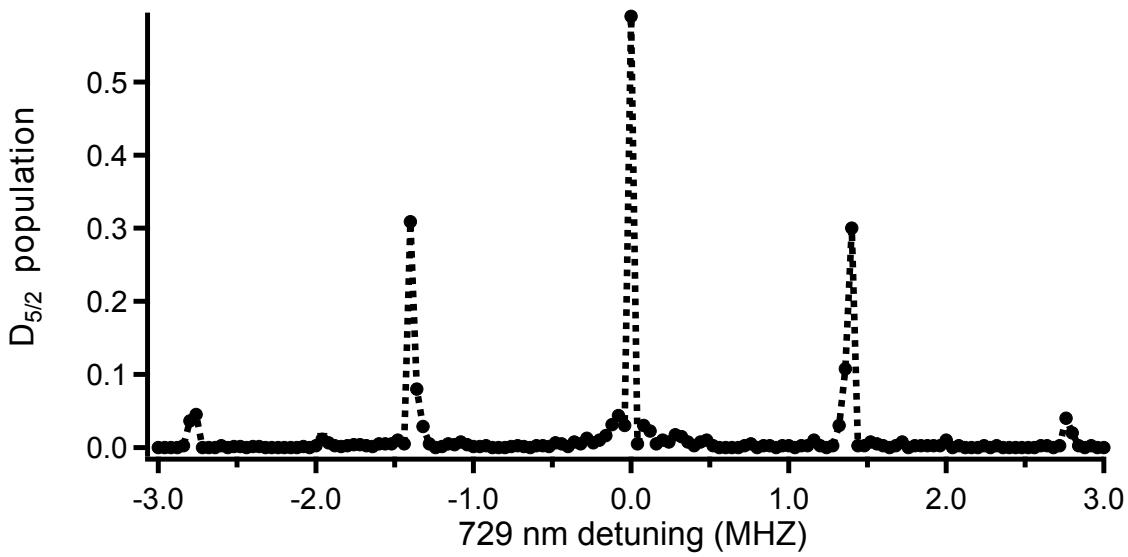

Figure 12: Frequency scan of the $S_{1/2} \rightarrow D_{5/2}$ transition over 6 MHz showing the carrier, both the first and second order red sidebands, and the first and second order blue sidebands. Reproduced from Ref. [20].

as in Fig. 13. Using a narrow-band laser such as the ones used in these experiments it is possible to find the resonant frequency of the $S_{1/2} \rightarrow D_{5/2}$ transition to tenths of kHz precision.

3.5 Spectroscopy of the $S_{1/2} \rightarrow D_{5/2}$ Line of $^{40}Ca^{+}$ While Moving the Ion Through a 729 nm Standing Wave

Once a standing wave has been formed on the surface of the ion trap with the 729 nm laser (Fig. 9), it becomes possible to suppress the odd order sidebands by placing the ion at a node. The even order sidebands and carrier transition can be suppressed by placing the ion at an anti-node. By tuning the frequency of the laser to either the carrier or first order sideband of the $S_{1/2} \rightarrow D_{5/2}$ transition while changing the compensation voltage applied to the center electrode, the ion is pushed through the standing wave moving from node to anti-node. If the $D_{5/2}$ population is monitored as a function of the applied electric field, then the nodes and anti-nodes can be mapped and the fringes of the standing wave become visible as shown in Fig. 14 where the carrier transition was addressed.

Although the scan shown in Fig. 14 is not a well resolved scan, a rough calculation of

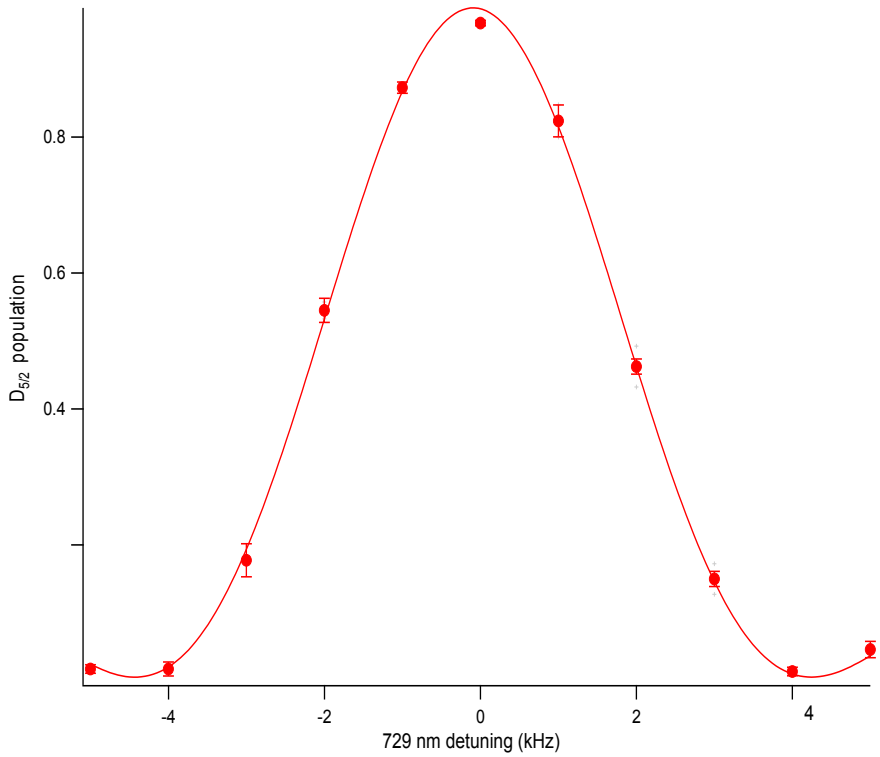

Figure 13: Frequency scan of the $S_{1/2} \rightarrow D_{5/2}$ transition as $D_{5/2}$ shelving vs. detuning of the 729 nm laser.

the interferometric visibility is possible and is carried out in Appendix B. This calculation gives the lower bound of the visibility of the standing wave to be 0.717.

To show that the carrier and sideband transitions are out of phase with each other, an ion position scan with the frequency of the 729 nm laser locked to the carrier transition was taken before taking another ion position scan with the frequency of the 729 nm laser locked to the first order blue sideband was taken. This is shown in Fig. 15. To change the position of the ion along the standing wave the voltage applied to the y compensation electrode was varied. Positive potentials applied to the compensation electrode pushed the positively charged ion closer to the laser while negative potentials pulled the ion closer to the trap.

Unfortunately, the π time was not updated between the carrier and sideband scans and thus the sideband compensation scan is very weak. For this reason Fig. 16 is included which plots the same data as in Fig. 15 but with a 4× amplification applied to the sideband

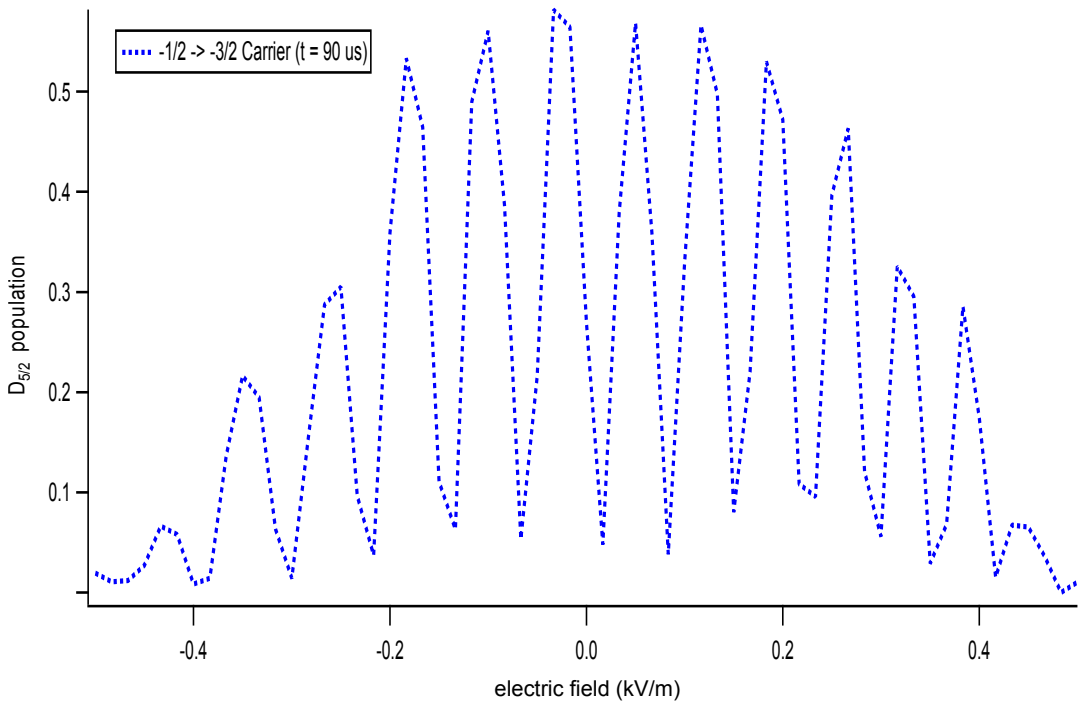

Figure 14: Ion position scan of the carrier transition. The electric field was varied from -500 V/m to 500 V/m, pushing the ion through the 729 nm standing wave, showing the nodes and anti-nodes. From the data in this plot the interferometric visibility was calculated in Appendix B.

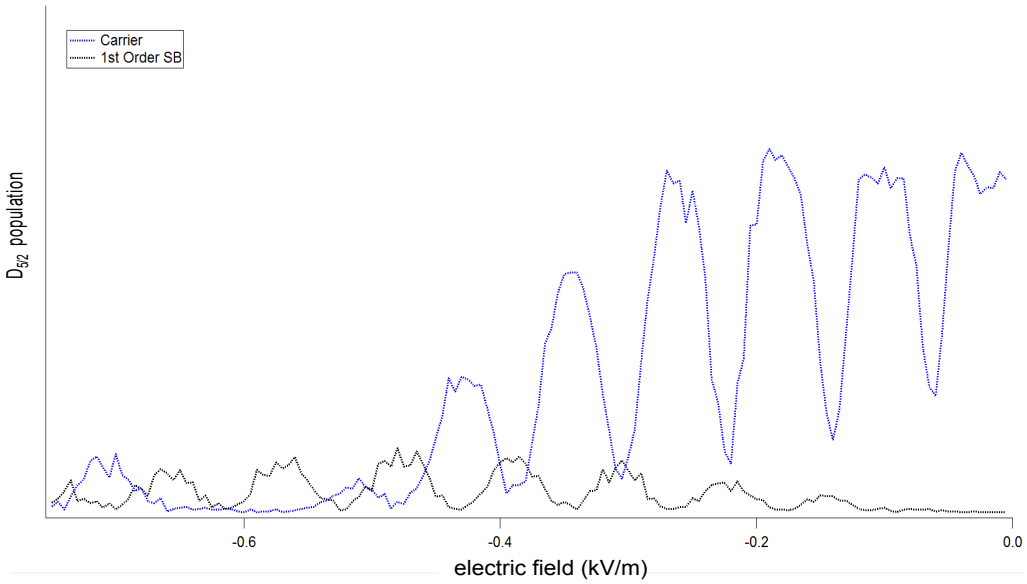

Figure 15: Scan of the voltage applied to the compensation electrode while monitoring the shelving of the $D_{5/2}$ state for the carrier and first order blue sideband.

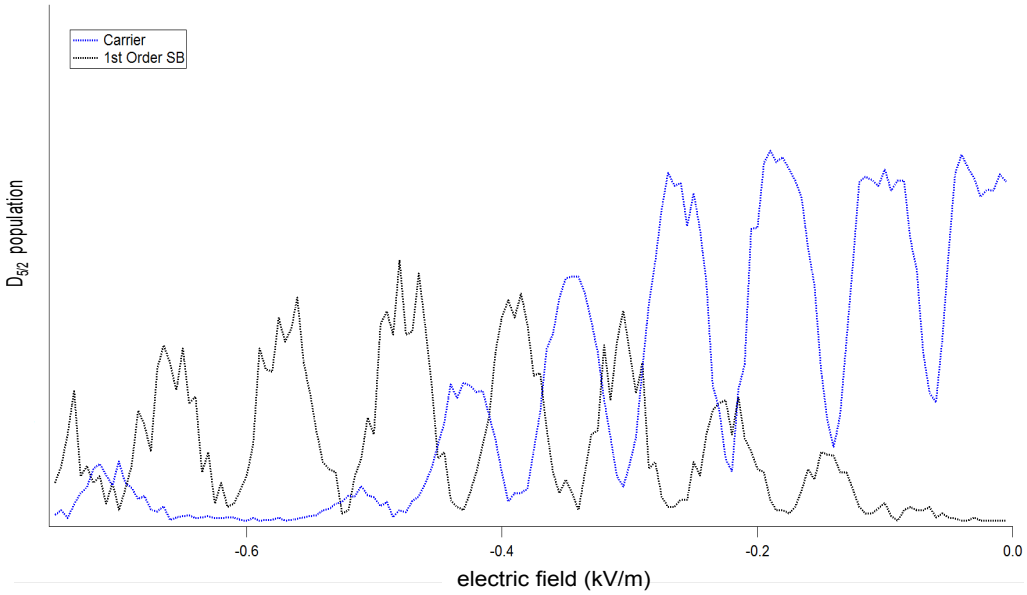

Figure 16: The same scan as shown in Fig. 15, but with a 4× amplification applied to the sideband points to better show the phases of the carrier and first order sideband scans.

points. This amplification makes it much easier to see the phase of the two scans and how they do not overlap.

CHAPTER IV

CONCLUSIONS AND APPLICATIONS

Trapped ions are able to serve as good qubits. By using a standing wave to address the qubit transition, ions exhibit interesting behavior concerning spatial modulation and the corresponding modulation of their Hamiltonians.

The most immediate impact of the standing wave studied in this thesis is its application to single qubit gates. With an ion positioned at an anti-node in a standing wave, the sidebands are suppressed and the electric field is amplified by a factor of 2 [46]. With the attenuated sidebands and electric field amplification, the rate at which single qubit gates such as the Hadamard gate, X gate, Y gate, or Z gate can be coherently performed is dramatically increased. The reason for this increase is two-fold. The first reason is the electric field amplification due to the added electric field of the reflection off the surface of the trap. The second reason is the attenuation of the sideband transitions. For example, the speed of the X gate applied to a $^{40}Ca^{+}$ qubit is generally not limited by the electric field amplitude but rather by decoherence due to power broadening of the carrier transition and off-resonant excitation of the motional sidebands [17]. By suppressing these sidebands, more power would be able to used and the speed of the X gate would be increased.

Another application of the standing wave is the Cirac-Zoller gate originally proposed in Ref. [5]. In this work, Cirac and Zoller specifically stated that the two qubit Controlled-NOT gate proposed should be performed in a standing wave in order to reduce off-resonant excitation of the carrier during blue sideband pulses. Although this gate has been realized experimentally [12, 13], it has never been performed with a standing wave. The two references listed did manage to suppress off-resonant excitation of the carrier transition by using low laser power, but this lead to lengthy calculation times which in turn lead to

higher heating rates and therefore less coherent gates. Were the Cirac-Zoller gate to be performed in a standing wave as suggested in the original proposal, the time required to perform the gate would be significantly decreased while the coherence of the gate would be greatly increased. The shorter gate time would lead to shorter times required to perform quantum algorithms while increased coherence would lead to fewer errors and therefore more accurate quantum calculations.

CHAPTER V

FUTURE WORK

Future experiments hope to better measure the interferometric visibility of the 729 nm standing wave by taking a higher resolution ion position scan like the one shown in Fig. 14. This higher resolution scan will put a tighter bound on the interferometric visibility. In addition, frequency scans of the 729 nm laser while the ion is positioned at a node (anti-node) will be taken in order to show the suppressed carrier (sideband) transition(s). These scans will be useful in determining the extent to which the Hamiltonian is able to be modified. Using the interferometric visibility and the heights of the carrier and sideband transitions at the nodes and anti-nodes of the standing wave, it should be able to calculate the attenuation and amplification capabilities of the modified Hamiltonian as compared to the Hamiltonian of an ion in a travelling wave. These suppressed sideband and carrier scans will also be used to simulate an analogue test of curved-spacetime quantum field theory effects as proposed in Ref. [29].

In addition to measuring the attenuation and amplification abilities and the interferometric visibility of the standing wave, future experiments hope to incorporate compensation fields throughout the course of a quantum algorithm. Just as the frequency and phase of a laser is changed while performing a quantum gate, the compensation field around an ion is be able to be changed. Previously, application of different compensation fields during a quantum gate would have served no purpose, but with the ability to suppress sideband or carrier transitions, applying different compensation fields would have the potential to better preserve the coherence of the electronic state of the trapped ion. By carefully mapping the nodes and anti-nodes of the standing wave by taking a a higher resolution scan of Fig. 15, it should be possible to integrate different compensation fields into a full quantum gate.

APPENDIX A

$S_{1/2} \rightarrow D_{5/2}$ FREQUENCY SHIFTS FOR DIFFERENT CA$^+$ ISOTOPES

The ability to address the $S_{1/2} \rightarrow D_{5/2}$ transition for different isotopes of calcium within a chain of trapped ions is of interest to both precision spectroscopy and quantum information experiments. For this reason, the frequency shifts of the 729 nm laser for different isotopes have been calculated and are shown in Table 1. This table is a reproduction of the data presented in Ref. [36] which shows the detuning of the 423 nm, 397 nm, and 866 nm lasers relative to the resonant transitions of ^{40}Ca$^+$. In addition, the calculated detuning of the 729 nm laser has been added.

Because of its natural abundance, all frequency shifts are calculated relative to ^{40}Ca$^+$. The particular calculation shown below is for the case of the second most abundant isotope ^{44}Ca$^+$ although all other isotope shifts were calculated in the same manner.

The calculation starts by forming a closed energy loop with the three $S_{1/2} \rightarrow D_{5/2}$ (729 nm), $D_{5/2} \rightarrow P_{3/2}$ (854 nm), and $P_{3/2} \rightarrow S_{1/2}$ (393 nm) transitions of both ^{40}Ca$^+$ and ^{44}Ca$^+$ shown in Fig. 3.

$$h\nu^{40}_{393\text{ nm}} - h\nu^{40}_{854\text{ nm}} - h\nu^{40}_{729\text{ nm}} = 0 \tag{1}$$

$$h\nu^{44}_{393\text{ nm}} - h\nu^{44}_{854\text{ nm}} - h\nu^{44}_{729\text{ nm}} = 0 \tag{2}$$

In these equations h is Planck's constant and ν^{40} and ν^{44} are the frequencies of the respective transitions for ^{40}Ca$^+$ and ^{44}Ca$^+$. Subtracting Eq. 1 from 2 yields

$$h\Delta\nu^{44}_{393\text{ nm}} - h\Delta\nu^{44}_{854\text{ nm}} - h\Delta\nu^{44}_{729\text{ nm}} = 0 \tag{3}$$

Here $\Delta\nu^{44}$ is the frequency detuning of the $^{44}Ca^{+}$ transition from the corresponding $^{40}Ca^{+}$ transition. The detuning values listed in Table 1 are now referenced and h is factored out, reducing the equation to

$$(842\ \text{MHz}) - (-4495\ \text{MHz}) - \Delta\nu^{44}_{729\ \text{nm}} = 0 \tag{4}$$

At this point, $\Delta\nu^{44}_{729\ \text{nm}}$ can be solved for and it is found that

$$\Delta\nu^{44}_{729\ \text{nm}} = 5337\ \text{MHz} \tag{5}$$

Adding this to the empirically determined value of $\nu^{40}_{729\ \text{nm}}$ gives

$$\nu^{44}_{729\ \text{nm}} = 411.04708(7)\ \text{THz} \tag{6}$$

The only experimental value of the 729 nm $S_{1/2} \rightarrow D_{5/2}$ transition for an isotope other than $^{40}Ca^{+}$ currently available in the literature is for $^{43}Ca^{+}$ and is found in Ref. [38]. According to this reference, the value of the calculated $S_{1/2} \rightarrow D_{5/2}$ shift for $^{43}Ca^{+}$ is off by only 19 MHz, or an error of 0.46%.

Table 1: Frequency shifts in MHz for different isotopes of Ca^+ relative to the most abundant isotope $^{40}Ca^+$. The data for the Ca $^1S_0 \rightarrow {}^1P_1$, Ca^+ $S \rightarrow P$, and Ca^+ $D \rightarrow P$ transitions are taken from Ref. [36] while the data for the Ca^+ $S \rightarrow D$ transition was calculated in the method shown in Appendix A.

		Isotope Shifts (MHz)			
Mass number	Natural abundance	Ca $^1S_0 \rightarrow {}^1P_1$ 423 nm	Ca^+ $S \rightarrow P$ 397 nm (393 nm)	Ca^+ $D \rightarrow P$ 854 nm (850, 866 nm)	Ca^+ $S \rightarrow D$ 729 nm (732 nm)
40	96.9%	0	0	0	0
42	0.647%	394	425(6)	-2350(4)	2775
43	0.135%	612	688(17)	-3465(4)	4153
44	2.09%	774	842(3)	-4495(4)	5337
46	0.004%	1160	1287(4)	-6478(8)	7765
48	0.187%	1513	1696(6)	-8288(7)	9984

APPENDIX B

CALCULATION OF THE INTERFEROMETRIC VISIBILITY OF THE 729 NM STANDING WAVE

To find the interferometric visibility of the 729 nm standing wave, the envelope of maximal and minimal carrier excitations shown in Fig. 14 are divided. This calculation assumes that the envelope function is linear between fringes. Although the envelope functions are not linear, the assumption is reasonable over short distances such as between the roughly 80 V/m spaced fringes.

The first step in the calculation is taking the points of maximal excitation at -33.3 V/m and 50 V/m

$$\text{Left Max} = 58.2\% \text{ shelving} \tag{7}$$

$$\text{Right Max} = 56.9\% \text{ shelving} \tag{8}$$

These two points are then averaged (this is where the linear scaling assumption is used) to find the what the excitation would be at 8.4 V/m compensation if the standing wave were to be shifted by 365 nm

$$\text{Max} = 57.6\% \text{ shelving} \tag{9}$$

The point of minimal excitation at 16.7 V/m is then found

$$\text{Min} = 4.78\% \text{ shelving} \tag{10}$$

Using Eq. 3.19 from Ref. [46] and substituting in the values of Max and Min provided in Eq. 9 and 10 gives the square root of the interferometric visibility.

$$\frac{\text{Max} - \text{Min}}{\text{Max} + \text{Min}} = \frac{57.6 - 4.78}{57.6 + 4.78} = 0.847 \tag{11}$$

In order to find the visibility it is necessary to take the square of this value because the Rabi frequency is dependent on the electric field amplitude while the visibility is dependent on the intensity which is proportional to the square of the electric field amplitude [28]. Taking the square of Eq. 11 gives

$$(0.847)^2 = 0.717 \tag{12}$$

This is equivalent to the interferometric visibility of the standing wave and thus

$$\mathcal{V} = 0.717. \tag{13}$$

This value of the interferometric visibility is a lower bound on the true value. The assumption of a linear envelope function decreases the height of the maximal excitation while the minimal excitation stays the same since only one point was used and no such assumption was made. In addition, the data used in this calculation was taken from a low resolution scan. If a higher resolution scan produced higher peaks and lower nulls (which is likely) then the visibility would be greater than 0.717.

REFERENCES

[1] R. P. Feynman, Int. J. Theor. Phys. **21** (1982). 1.1

[2] P. W. Shor, in *Ann. IEEE Symp. Found.*, IEEE Press, 1994. 1.1

[3] L. K. Grover, Phys. Rev. Lett. **79**, 325 (1997). 1.1

[4] A. Aspuru-Guzik, A. D. Dutoi, P. J. Love, and M. Head-Gordon, Science **309**, 1704 (2005). 1.1

[5] J. I. Cirac and P. Zoller, Phys. Rev. Lett. **74**, 4091 (1995). 1.1, 1.4, 4

[6] J. J. Bollinger, D. J. Wineland, W. M. Itano, and J. S. Wells, AIP Conf. Proc. (1983). 1.2

[7] J. J. Bollinger, W. M. Itano, and D. J. Wineland, Proc. 37th Ann. Symp. Freq. Control (1983). 1.2

[8] S. R. Jefferts, C. Monroe, A. S. Barton, and D. J. Wineland, IEEE Trans. Instrum. Meas. **44** (1995). 1.2

[9] J. J. Bollinger, D. J. Henizen, W. M. Itano, S. L. Gilbert, and D. J. Wineland, Proc. 12th Intl. Conf. on Atomic Physics (1990). 1.2

[10] U. Eichmann *et al.*, Phys. Rev. Lett. **70**, 2359 (1993). 1.2

[11] D. J. Wineland, J. J. Bollinger, D. J. Heinzen, W. M. Itano, and M. G. Raizen, Phys. Rev. Lett. **67**, 1735 (1991). 1.2

[12] F. Schmidt-Kaler *et al.*, Nature **422**, 408 (2003). 1.2, 4

[13] M. Riebe *et al.*, Phys. Rev. Lett. **97**, 220407 (2006). 1.2, 4

[14] D. P. DiVincenzo, arXiv:quant-ph/0002077v3 (2000). 1.2

[15] J. Labaziewicz *et al.*, Phys. Rev. Lett.. **100**, 013001 (2008). 1.2, 1.3, 1.4

[16] H. Haffner, C. F. Roos, and R. Blatt, Phys. Rep. **469**, 155 (2008). 1.2, 2.2.2, 3.3

[17] W. C. Campbell *et al.*, Phys. Rev. Lett. **105**, 090502 (2010). 1.2, 4

[18] J. Chiaverini *et al.*, Quantum Inform. Compu. **5**, 419 (2005). 1.2

[19] Q. A. Turchette *et al.*, Phys. Rev. A **61**, 063418 (2000). 1.2

[20] G. Vittorini, *Stability of Ion Chains in a Cryogenic Surface-Electrode Ion Trap*, Thesis, 2013. 1.3, 2.2.2, 2.3, 8, 3.1, 12

[21] D. J. Wineland *et al.*, J. Res. Natl. Inst. Stan. **103**, 259 (1998). 1.3, 2.3

[22] D. A. Hite *et al.*, Phys. Rev. Lett. **109**, 103001 (2012). 1.3

[23] J. Chiaverini and J. M. Sage, Phys. Rev. A **89**, 012318 (2014). 1.3, 1.4

[24] M. Niedermayr *et al.*, arXiv:1403.5208 [quant-ph] (2014). 1.3

[25] M. E. Poitzsch, J. C. Bergquist, W. M. Itano, and D. J. Wineland, Rev. Sci. Instrum. **67**, 129 (1996). 1.3

[26] G. Vittorini, K. Wright, K. R. Brown, A. W. Harter, and S. C. Doret, Rev. Sci. Instrum. **84**, 043112 (2013). 1.3, 1.4, 1.4, 2.1

[27] S. C. Doret *et al.*, New J. Phys. **14**, 073012 (2012). 1.4, 2.1, 2.4

[28] Y. B. Band, *Light and Matter: Electromagnetism, Optics, Spectroscopy, and Lasers* (Wiley, 2006). 1.4, B

[29] N. C. Menicucci, S. J. Olson, and G. J. Milburn, New J. Phys. **12**, 095019 (2010). 1.4, 5

[30] G. W. Gibbons and S. W. Hawking, Phys. Rev. D **15**, 2752 (1977). 1.4

[31] G. Ver Steeg and N. C. Menicucci, Phys. Rev. D **79**, 044027 (2009). 1.4

[32] P. K. Ghosh, *Ion Traps* (Clarnedon Press, 1995). 2

[33] J. T. Merrill, *Compensating Sequences for Robust Quantum Control of Trapped-Ion Qubits*, Thesis, 2013. 2

[34] P. Richerme, *Depletion, Quantum Jumps, and Temperature Measurements of* $^{88}Sr^{+}$ *Ions in a Linear Paul Trap*, Thesis, 2013. 2

[35] C. J. Foot, *Atomic Physics* (Oxford University Press, 2005). 2

[36] D. M. Lucas *et al.*, Phys. Rev. A **69**, 012711 (2004). 2.1, 2.1.1, 3.3, A, 1

[37] D. J. Berkeland, J. D. Miller, J. C. Bergquist, W. M. Itano, and D. J. Wineland, J. Appl. Phys. **83**, 5025 (1998). 2.1

[38] J. Benhelm *et al.*, Phys. Rev. A **75**, 032506 (2007). 2.1.1, A

[39] H. J. Metcalf and P. van der Straten, *Laser Cooling and Trapping* (Springer, 2001). 2.2.1

[40] R. Hendricks, J. Sorensen, C. Champenoid, M. Knoop, and M. Drewsen, Phys. Rev. A **77**, 021401 (2008). 2.2.1

[41] J. Goeders, *Resolved Sideband Spectroscopy for the Detection of Weak Optical Transitions*, Thesis, 2013. 2.2.1

[42] J. Eschner, G. Morigi, F. Schmidt-Kaler, and R. Blatt, J. Opt. Soc. Am. B **20**, 1003 (2003). 2.2.1

[43] C. Roos *et al.*, Phys. Rev. Lett. **83**, 4713 (1999). 2.2.2, 2.2.2

[44] Quantum Information Systems Group at the Georgia Tech Research Insitute, *Gen II Linear Trap Operation Manual*. 2.2.2, 3.4

[45] A. Kramida, Y. Ralchenko, J. Reader, and the NIST ASD Team, `http://physics.nist.gov/asd` ver. 5 (2012). 2.3

[46] G. R. Fowles, *Introduction to Modern Optics* (Dover, 1989). 2.4, 4, B

[47] Brimrose Corporation of America, *Introduction to Acousto-Optics*. 3.2

[48] K. J. Boller, A. Imamoglu, and S. E. Harris, Phys. Rev. Lett. **66**, 2593 (1991). 3.3

[49] L. Slodicka, G. Hetet, S. Gerber, M. Hennrich, and R. Blatt, Phys. Rev. Lett. **105**, 153604 (2010). 3.3

[50] G. Morigi, J. Eschner, and C. H. Keitel, Phys. Rev. Lett. **85**, 4458 (2000). 3.3

[51] F. Schmidt-Kaler *et al.*, Appl. Phys. B-Lasers O. **73**, 807 (2001). 3.3

[52] Y.-W. Lin, S. Williams, and B. Odom, Phys. Rev. A **87**, 1210.0551 (2013). 3.3